IS-PORTO 2023 PROCEEDINGS

Proceedings of the 8th International Symposium on DEFORMATION CHARACTERISTICS OF GEOMATERIALS Porto, 3rd - 6th September 2023

Exploring the role of fabric anisotropy in cyclic liquefaction resistance under non-hydrostatic consolidation: insights from DEM analysis

Ming Yang[1] and *Mahdi* Taiebat[2#]

[1]*Northwestern University, Department of Civil and Environmental Engineering, Evanston, IL, USA*
[2]*University of British Columbia, Department of Civil Engineering, Vancouver, BC, Canada*
[#]*Corresponding author: mtaiebat@civil.ubc.ca*

ABSTRACT

This study investigates the cyclic liquefaction resistance of granular materials under non-hydrostatic consolidation using 3D discrete element method (DEM) simulations. The study specifically examines how various sample preparation techniques affect the cyclic liquefaction resistance of polydisperse spherical particle samples with a Kc value of 0.5, where Kc represents the ratio of initial horizontal to vertical normal stresses. The results reveal that the choice of sample preparation technique significantly affects the cyclic liquefaction resistance of the samples. Furthermore, this study explores the inherent fabric of the samples using coordination number and contact-normal fabric anisotropy, and demonstrates that it plays a critical role in controlling the cyclic liquefaction resistance of granular materials under non-hydrostatic consolidation. The study emphasizes the significance of considering the inherent fabric in understanding the behavior of granular materials under non-hydrostatic consolidation. This can inform the design of experiments and the development of constitutive models to explore the interplay between sample preparation techniques, fabric anisotropy, and cyclic liquefaction resistance.

Keywords: granular materials; non-hydrostatic consolidation; liquefaction resistance; inherent fabric.

1. Introduction

When subjected to constant volume cyclic shearing, granular soils initially exhibit a solid-like response. However, continued cyclic shearing may cause them to lose their shear strength and exhibit a fluid-like response transiently, resulting in a loss of ability to provide bearing support for civil infrastructure. This phenomenon, known as cyclic liquefaction, has been widely recognized as a cause of catastrophic damage during strong earthquake shaking. Therefore, cyclic liquefaction has been extensively studied in the past few decades to identify the factors that influence the liquefaction resistance of granular soils. These factors can be broadly divided into two categories, namely (1) particle-level properties such as particle shape and particle size distribution, and (2) sample homogenized properties such as density, stress state, and inherent fabric. Among these factors, inherent fabric, which is influenced by sample preparation protocols, has drawn substantial attention from researchers that attempt to uncover the mysterious veil given the measurement difficulty in the laboratory and its significant influence on the mechanical response of granular materials.

Soil fabric refers to the arrangement of particles, particle groups, and pore spaces in the particle assembly (Mitchell and Soga 2005). More specifically, spatial distributions of particle long axes, contact-normals, branch vectors, and pore shapes, have been used to explicitly quantify soil fabric, resulting in different types of fabric characterizations. The variations in these fabric descriptors due to different sample preparation methods in the laboratory setup, such as wet sedimentation, air pluviation, and moist tamping, have been considered to explain the observed differences in the macroscopic stress-strain behaviors (e.g., Mulilis et al. 1977; Tatsuoka et al. 1982; Yamashita and Toki 1993; Oda et al. 2001; Vaid and Sivathayalan 2000; Wood et al. 2008; Ni et al. 2022). For instance, samples prepared by wet-tamping present noticeably higher liquefaction strength than those prepared using dry vibration or air pluviation (Mulilis et al. 1977; Tatsuoka et al. 1982). However, these findings are mainly descriptive or qualitative due to the difficulty in determining the fabric quantities unless special experimental techniques such as computed tomography and image analysis (Yang et al. 2008, Ni et al. 2021) are used.

In contrast to the inconvenience of extracting the laboratory sample fabric, discrete element method (DEM), as a numerical approach modeling interparticle interactions, stores all the particle information and allows flexible analysis of particle arrangement. Several recent studies have used DEM to characterize and assess the signatures of cyclic liquefaction (e.g., Wang and Wei 2016; Hung et al. 2019; Yang et al. 2021, 2022a, 2022b). The effects of initial fabric on the cyclic liquefaction response of granular materials have also been explored by focusing on factors such as the particle size distribution (Banerjee et al. 2023), elongated particle orientations (Zhang et al. 2023), and coordination number and contact normal fabric anisotropy (Wei and

Wang 2017; Otsubo et al. 2022), to name a few. For example, Zhang et al. (2023) observed that the samples with dominant vertical particle orientation are more prone to liquefaction under cyclic triaxial shearing. Wei and Wang (2017) pointed out that samples with higher coordination numbers and lower fabric anisotropies present higher liquefaction strength in simple shear tests. Otsubo et al. (2022) concluded that triaxial samples with the same coordination number exhibit reduced liquefaction resistance with increasing fabric anisotropy.

It should be noted that the samples constructed in the above-mentioned studies embrace an initial isotropic stress state. This paper aims to extend the investigation of initial fabric effects to the DEM samples prepared following an anisotropic consolidation. Here, anisotropic consolidation ratio is introduced, denoted as K_c and representing the initial horizontal and vertical normal stresses ratio. Three different sample preparation protocols are adopted to construct DEM samples with $K_c = 0.5$ and subject these samples to constant-volume cyclic simple shearing to determine the liquefaction resistance. The sample initial fabric will be quantified by coordination number and contact-normal fabric anisotropy, which will be used to explain the observed distinct simulation results by correlating with the liquefaction resistance.

2. DEM setup

The open-source DEM code LIGGGHTS (Kloss et al. 2012) is used to simulate particle dynamics in this study. Spherical particles are adopted to construct the granular assembly composed of 15625 polydisperse particles, divided into ten discrete subclasses with distinct particle sizes, that follow the particle size distribution of Ottawa-F65 sand, as shown in Fig. 1. Details of generating the particle size distribution can be found in Taiebat et al. (2017) and Mutabaruka et al. (2019). The particles interact based on soft-particle laws, allowing slight overlap at the contact point, including a Hertzian normal model, a history-dependent tangential model with a Coulomb friction cut-off, and the modified elastic-plastic spring dashpot model (EPSD3) as the rolling model. Details of the contact models can be found in LIGGGHTS documentation. The DEM model parameters, including particle density ρ, particle Young's modulus E, Poisson's ratio ν, coefficient of restitution ε, tangential friction coefficient μ, and rolling friction coefficient μ_r, are provided in Table 1. LIGGGHTS adopts an explicit velocity-Verlet time-stepping scheme to update positions and velocities of spherical particles. The time step size $\Delta t = 2 \times 10^{-9}$ s is determined to be less than 5% of the Rayleigh (wave propagation time scale) and Hertz (contact time scale) time step sizes, ensuring enough accuracy of the numerical integration.

The simulation involves two main phases: (1) constructing DEM sample via anisotropic compression to the target mean stress $p_0 = 100$ kPa and (2) applying cyclic simple shearing to the sample under constant-volume condition.

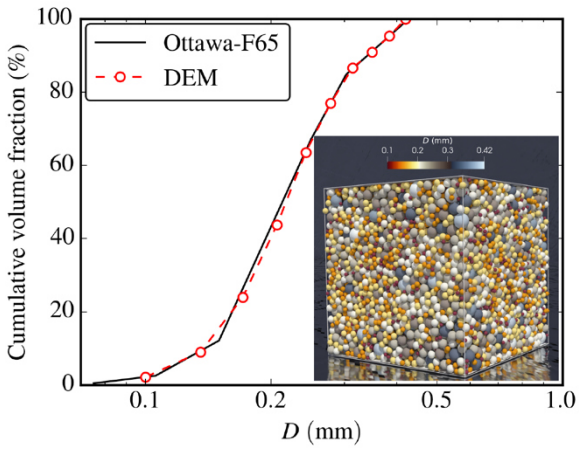

Figure 1. Particle size distributions with the inset snapshot of the simulated DEM sample composed of 15625 polydisperse spherical particles

2.1. Sample preparation

In the sample preparation phase, the particles are initially randomly placed on a three-dimensional (3D) sparse lattice of $25 \times 25 \times 25$ to avoid overlap. This 3D lattice is contained in a rectangular cell with all six sides being rigid walls. The sample is then compressed by translating the six sides of the cell to achieve the final target stress state, following four stages of sample preparation outlined in Yang et al. (2021): (1) using a small tangential friction coefficient $\mu = \mu_I$, densifying the sparse cell by moving the six rigid walls at a constant small velocity until the void ratio e reaches 1.2; (2) setting the velocities of the six rigid walls to zero and using a servo-control algorithm to compress the sample isotopically to the target mean stress $p = 0.1p_0$ with the same μ_I; (3) replacing the four lateral sides with periodic boundaries, increasing the target mean stress to $0.2p_0$, and continuing isotropic compression with the same μ_I; (4) modifying μ to 0.5 for further compressing the sample anisotropically to the final target mean stress p_0, where the target vertical normal stress $\sigma_{v0} = 1.5p_0$ and target horizontal normal stress $\sigma_{h0} = 0.75p_0$. The four-stage sample preparation protocol is denoted as protocol A (PA). The first three rows in Table 2 list the samples prepared following PA, including a dense (D), a medium dense (M), and a loose (L) packing. The maximum and minimum void ratios, namely e_{max} and e_{min} mentioned in Table 1, are determined from PA samples prepared using $\mu_I = 0$ and 0.5, respectively.

Another sample preparation protocol is introduced denoted as protocol B (PB) to reduce the high contact densities observed in the PA-D sample but maintain similar void ratios. PB follows the same four stages of sample construction as PA but adds a fifth stage with $\mu = 0.5$ that involves applying a homogenous expansion (Agnolin and Roux 2007) and a subsequent anisotropic compression: first, all coordinates of particles are multiplied by a common factor λ slightly larger than 1, then random velocities in the range of $\pm v_I$ in each spatial direction are assigned to particles, and servo-control algorithm is finally applied to perform anisotropic compression to reach the target stress state. Three PB samples are prepared using $\lambda = 1.0005$ and $v_I = 0.02$ m/s, as presented in Table 2.

Table 1. DEM parameters

Description	Symbol	Value
Particle density	ρ	2650 kg/m^3
Young's modulus	E	70 GPa
Poisson's ratio	ν	0.25
Coefficient of restitution	ε	0.8
Tangential friction coefficient	μ	0.5
Rolling friction coefficient	μ_r	0.1

In addition to PB, another protocol referred to as protocol C (PC) is adopted to reduce the high contact density mainly in the PA dense samples because of the use of small μ_{I}. The PC follows the same four stages of PA, with the only difference being in stage (2): a moderate μ_{I} combined with assigning random velocities to particles in all three spatial directions at every certain number of simulation steps n_{stage}. Each random velocity component is in the $\pm v_{\mathrm{I}}$ range. The choices of μ_{I}, v_{I} and n_{stage} will determine the final packing density of the DEM sample, requiring iterative trials to prepare PC samples with similar densities as the PA ones. The last three rows in Table 2 present the constructed PC samples, where $v_{\mathrm{I}} = 0.13$, 0.07, and 0.03 m/s are used to obtain dense, medium dense, and loose samples, respectively, with $n_{\mathrm{stage}} = 10^5$.

Table 2. Properties of DEM samples at $p_0 = 100$ kPa ($e_{\max} \simeq 0.669$, $e_{\min} \simeq 0.510$)

Sample ID	μ_{I}	e_0	$D_{\mathrm{r}}(\%)$	z_{m0}	a_{c0}
PA-D	0.1	0.586	52.2	5.45	0.06
PA-M	0.2	0.620	30.8	4.67	0.17
PA-L	0.4	0.653	10.1	4.33	0.37
PB-D	0.1	0.585	52.8	4.66	0.18
PB-M	0.2	0.614	34.6	4.39	0.26
PB-L	0.4	0.630	24.5	4.29	0.34
PC-D	0.4	0.589	50.3	4.59	0.28
PC-M	0.4	0.622	29.6	4.45	0.29
PC-L	0.45	0.648	13.2	4.34	0.34

Two micromechanical contact-based indicators, namely the mechanical coordination number z_{m} and fabric anisotropy a_{c}, are adopted in this study to quantify the inherent fabric of DEM samples. z_{m} is defined as the average number of contacts per particle, excluding particles with zero and one contact as these particles do not contribute to expanding force network (Thornton 2000):

$$z_{\mathrm{m}} = \frac{2N_c - N_p^1}{N_p - N_p^0 - N_p^1} \tag{1}$$

where N_c is the number of contacts, N_p is the number of particles, and N_p^0 and N_p^1 are the numbers of particles with zero and one contact, respectively. a_{c} represents the deviatoric invariant of the fabric anisotropy tensor $\boldsymbol{a}_{\mathrm{c}}$, quantifying the orientation of contact network:

$$a_c = \sqrt{\frac{3}{2}\boldsymbol{a}_c : \boldsymbol{a}_c} \tag{2}$$

$$\boldsymbol{a}_c = \frac{15}{2}\left(\boldsymbol{\phi}_c - \frac{1}{3}\boldsymbol{I}\right) \tag{3}$$

$$\boldsymbol{\phi}_c = \frac{1}{N_c}\sum_{c \in N_c} \boldsymbol{n} \otimes \boldsymbol{n} \tag{4}$$

Here $\boldsymbol{I}$ is the second-order identity tensor, $\boldsymbol{\phi}_c$ is the fabric tensor related to contact normal $\boldsymbol{n}$ (Oda 1982), and $\otimes$ denotes the tensor dyadic product.

The initial values of z_{m} and a_{c} for samples prior to shearing are provided in Table 2, and their variations with relative density D_{r} are presented in Fig. 2. Apparently, z_{m0} increases and a_{c0} decreases with increasing D_{r} for all samples. PA medium dense and dense samples generally exhibit higher z_{m0} and lower a_{c0} compared with PB and PC ones, confirming that PA specimens at higher D_{r} tend to have high contact densities. These packing properties will be reflected by the cyclic liquefaction response of the samples, as revealed later.

2.2. Simple shearing

In the constant-volume cyclic simple shearing phase, the sample volume is kept constant by fixing four lateral sides and the bottom wall and keeping the sample height constant. Cyclic simple shearing is undertaken by moving the top wall horizontally at a constant velocity v_x. To reduce possible slippage between the walls and the sample, a layer of particles is glued to the top and bottom walls, respectively, as shown in Fig. 3. The kinematics of these particles only follow the imposed velocity on the walls. The shear direction is reversed each time that shear stress magnitude, obtained from the calculated stress tensor, reaches a target amplitude τ^{amp}. The cyclic shearing intensity is quantified by the dimensionless quantity cyclic stress ratio (CSR), defined as $\mathrm{CSR} = \tau^{\mathrm{amp}}/p_0$.

The appropriate shear rate is determined by evaluating the inertial number $I = \dot{\gamma}\,\bar{d}\sqrt{\rho/p}$, where $\dot{\gamma} = |v_x|/h$ denotes the shear rate, h is the sample height, and $\bar{d}$ is the mean particle diameter. The inertial number I represents the shear rate normalized by the relaxation rate under the action of the mean stress p. The shearing is quasistatic if $I < 10^{-3}$. When the sample liquefies, the mean stress p degrades to vanishingly small values due to unjamming, which may cause I to increase beyond 10^{-3} regardless of its value before liquefaction. This study sets $\dot{\gamma}$ as $1\ \mathrm{s}^{-1}$ to increase simulation speed while maintaining quasistatic shearing during jammed states of the sample. The higher values of I at unjamming occur as a result of unstable deformation and sudden decrease of p, which is an intrinsic feature of cyclic liquefaction only and not influenced by the loading rate (Yang et al. 2021).

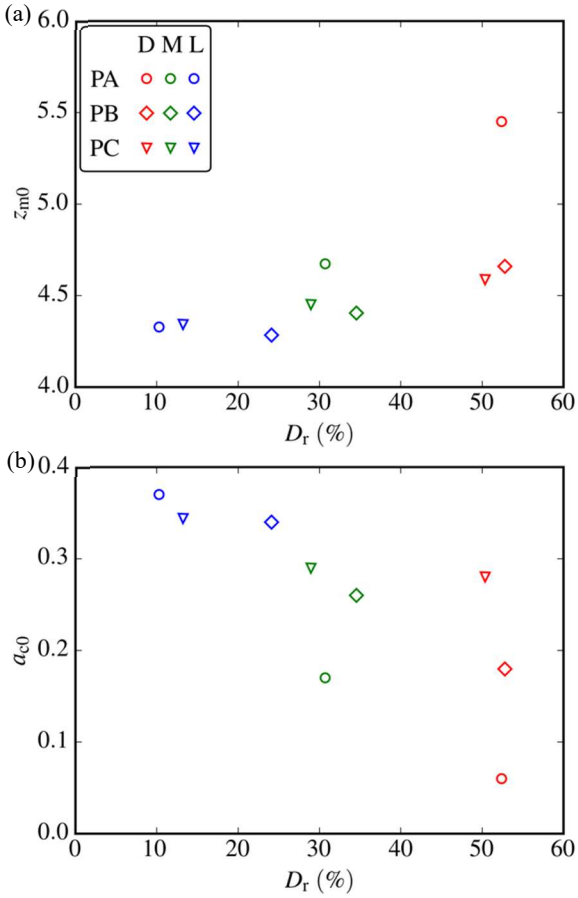

Figure 2. Variations of (a) initial mechanical coordination number z_{m0} and (b) initial contact normal-based fabric anisotropy a_{c0}, of the samples with the relative density D_r.

3. Simulation results

The stress tensor $\boldsymbol{\sigma}$ of the DEM sample is determined from the contact forces and particle positions over a selected volume V:

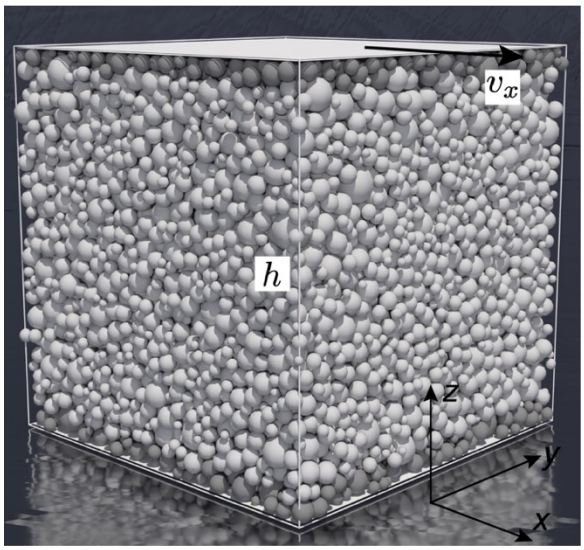

Figure 3. Illustration of particle arrangement and boundary conditions for DEM sample during constant height simple shearing. The dark particles are glued to the top and bottom walls of the simulation cell.

$$\boldsymbol{\sigma} = \frac{1}{V}\sum_{c\in N_c} \boldsymbol{l}^c \otimes \boldsymbol{f}^c \tag{5}$$

where $\boldsymbol{l}^c$ is the branch vector connecting the centers of two particles for interior contact or connecting the particle center and the contact point for exterior contact, $\boldsymbol{f}^c$ is the contact force, and the summation runs over all the contacts N_c belonging to V. In the simple shear test, the shear stress τ and mean effective stress p are given by $\tau = \sigma_{xz}$ and $p = (\sigma_{xx} + \sigma_{yy} + \sigma_{zz})/3$, respectively.

Pore water is not explicitly modelled in the DEM simulations. The excess pore pressure in the equivalent truly undrained system can be deduced from the variation $\Delta u = p_0 - p$ of the pore pressure, referring to the amount of load not supported by the particles and therefore supported by the saturating fluid. The excess pore pressure ratio is given by $r_u = \Delta u/p_0 = 1 - p/p_0$. The shear strain γ is the ratio of x_w/h, where x_w is the cumulative horizontal displacement of the top wall. The number of cycles N is used as a time variable instead of running time t, where a fractional cycle number is defined by interpolation between two successive cycles. A cycle starts with $\gamma = 0$, approaches a quarter when γ reaches the positive amplitude, becomes a half when γ drops back to zero, and attains the third quarter with a negative amplitude of γ.

3.1. Stress and strain response

Figure 4 displays the simulated macroscopic response of PA samples subjected to constant-volume cyclic simple shearing, including stress path, stress-strain loops, excess pore pressure evolution, and shear strain development. All three simulations start from $p = 100$ kPa, $\tau = 0$ kPa, and $\gamma = 0$. In the cyclic shearing process, τ oscillates between $-\tau^{\text{amp}}$ and τ^{amp}. Initially, the value of p gradually decreases with each cycle. After some cycles, p gradually stabilizes and enters a transition phase. During this phase, after each period of dilation (reflected in an increasing trend of p), a period of contraction occurs at an accelerating rate upon reversal of shearing and under relatively small changes of shear strains.

The term used to describe the first time that p drops to very small values, e.g., below 1 kPa, or r_u reaches 0.99, is initial liquefaction. N_{IL} is the corresponding number of cycles and is used to describe cyclic liquefaction resistance. The shear process before and after the initial liquefaction are referred to as pre- and post-liquefaction periods, respectively, which are highlighted in light and dark colors in Fig. 4. The post-liquefaction stress path gets trapped in a typical butterfly shape, and the stress-strain loops keep expanding at each cycle – a manifestation of the so-called cyclic mobility, as shown in Fig. 4(a)(b)(d)(e) for the PA-D and PA-M samples. The stress path of PA-L sample in Fig. 4(c) indicates that the internal shear stress cannot reach the specified τ^{amp} in two loading cycles, as highlighted by the star marker. This phenomenon, which is called cyclic

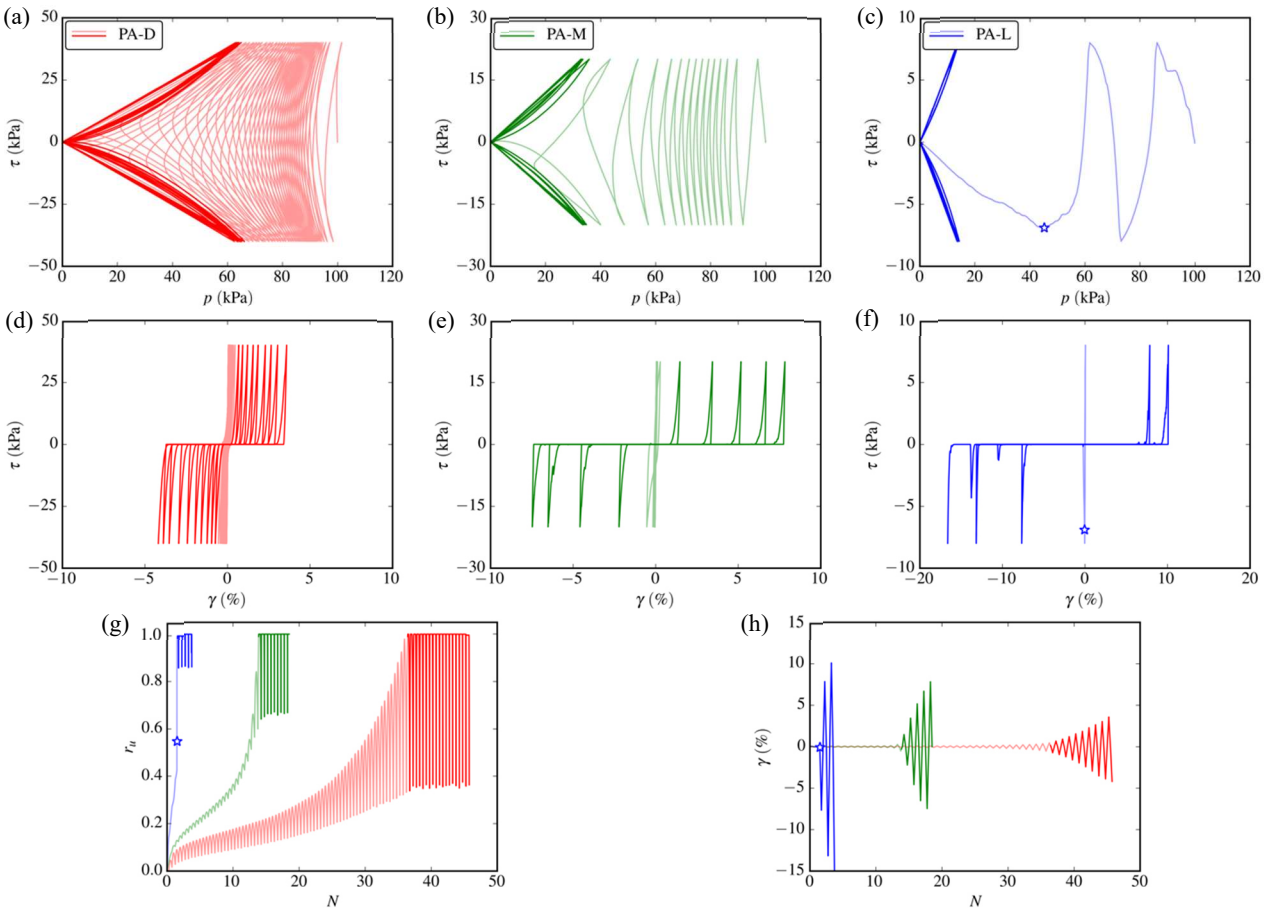

Figure 4. Macroscopic response of constant-volume cyclic simple shear tests on DEM samples of (a)(d) PA-D, (b)(e) PA-M, and (c)(f) PA-L, and comparisons of simulation results in (g) excess pore pressure evolutions and (h) shear strain developments.

instability and followed by flow liquefaction, is widely observed in loose saturated sands under dynamic shaking.

Figure 4(g) reveals an increasing trend in r_u oscillation magnitude with increasing D_r, which is due to the applied higher τ^{amp} that ensures liquefaction of these samples in the reasonable number of cycles. One should note the elevated increments of shear strain amplitudes in the post-liquefaction cycles for the medium dense and loose samples compared to the dense one, as also revealed in the laboratory experiments and other DEM simulations (e.g., Wang and Wei 2016).

There is no distinct difference in the macroscopic response among PA, PB, and PC samples, so the simulation results of PB and PC samples are not presented here for brevity.

3.2. Cyclic liquefaction resistance

This study defines cyclic liquefaction failure as the state of initial liquefaction, which can be triggered by different combinations of the uniform CSR and the number of loading cycles. The liquefaction strength curve, i.e., the plot of CSR versus the number of cycles to initial liquefaction N_{IL}, is used to describe the liquefaction resistance of the sample.

Figure 5 presents the liquefaction strength curves of all nine samples, where each data point corresponds to a constant-volume cyclic simple shear test on a sample subjected to a given uniform CSR. The discrete data points related to the same sample are fitted by a power-law function, namely $\mathrm{CSR} \propto N_{\mathrm{IL}}^{-b}$, with b being a fitting parameter. The different samples at similar D_{r} present rather nearly parallel liquefaction strength curves, suggesting a decreasing trend in the liquefaction strength of dense and medium-dense samples following the order of PA, PB, and PC. PB-L presents noticeably higher liquefaction resistance than PA-L and PC-L, which can be attributed to the densification of the sample during the fifth stage of sample preparation, since PB-L has a higher D_{r}, as shown in Table 2.

The cyclic resistance ratio (CRR) is introduced to quantify the liquefaction strength, corresponding to the value of CSR that induces initial liquefaction at 20 loading cycles. The CRR values are extracted from the fitted liquefaction strength curves. Figure 6 presents variations of CRR against relative density, where the data points from the same sample preparation protocol are fitted by an exponential function, i.e., $\mathrm{CRR} \propto \exp mD_{\mathrm{r}}$, with m being the fitting parameter. Figure 6 conveys the same message as Fig. 5: the effect of sample preparation protocols adopted in this study on cyclic liquefaction resistance is more pronounced in samples with higher

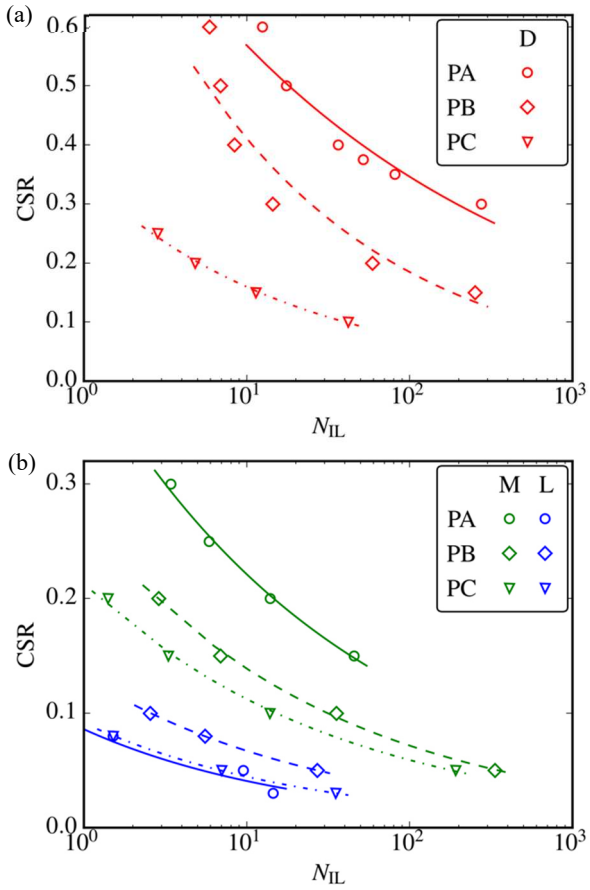

Figure 5. Liquefaction strength curves of (a) dense and (b) medium dense and loose samples, for the three sample preparation protocols PA, PB, and PC.

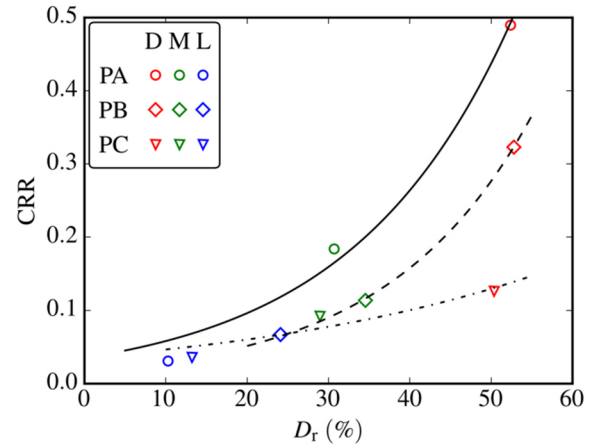

Figure 6. Variations of cyclic resistance ratio (CRR) against relative density (D_r) for the three sample preparation protocols PA, PB, and PC.

relative densities. Additionally, one should notice the nearly parallel curves for PA and PB samples, different from the PC curve, indicating the fifth-stage homogenous expansion adopted in PB affects the samples in a consistent way with respect to D_r when compared to PA.

3.3. Linking with the initial state

The observed difference in CRR values of medium dense and dense samples prepared following different

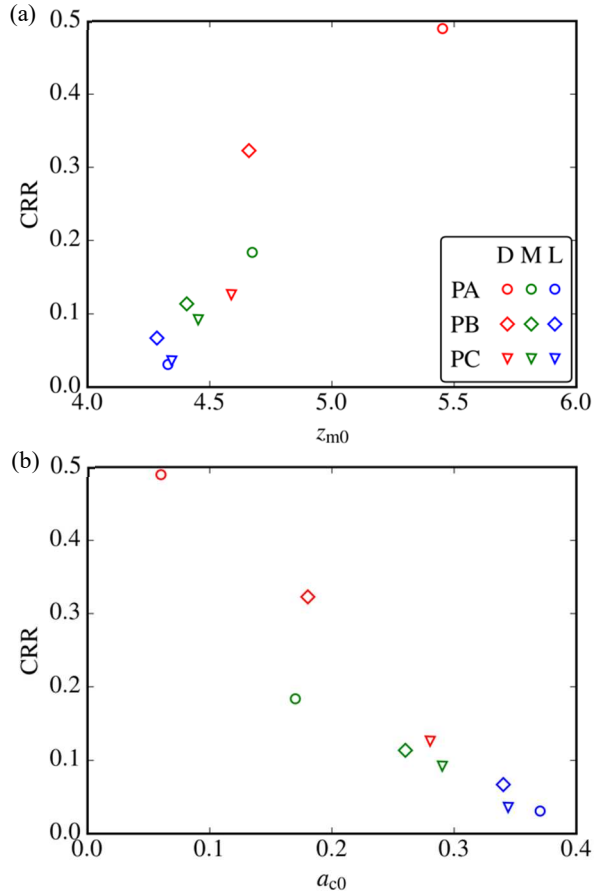

Figure 7. Variations of cyclic resistance ratio (CRR) against (a) initial mechanical coordination number and (b) initial contact normal fabric anisotropy.

sample preparation protocols is attributed to the initial fabric prior to cyclic shearing. In this study, the initial mechanical coordination number z_{m0} and contact-normal fabric anisotropy a_{c0} are used as descriptors of the initial fabric. Figure 7 displays the variations of CRR values against z_{m0} and a_{c0}, indicating a general trend that CRR increases with increasing z_{m0} or decreasing a_{c0}. This observation is consistent with recent DEM studies (Wei and Wang 2017; Gu et al. 2020; Otsubo et al. 2022). The reducing liquefaction strength from PA, PB to PC can be attributed to the decreasing z_{m0} or increasing a_{c0} for the samples at higher D_r. However, this explanation does not apply to the loose samples, since they have similar z_{m0} and a_{c0}, but PB-L presents clearly higher liquefaction resistance. Further analysis of the fabric tensor components or other fabric descriptors may be necessary to provide an adequate explanation.

4. Conclusion

In this study, 3D-DEM constant-volume cyclic simple shear simulations are conducted to investigate the effect of the initial fabric on the cyclic liquefaction resistance of anisotropically consolidated samples. To prepare DEM samples consisting of polydisperse spherical particles, three different sample preparation protocols (PA, PB, and PC) were adopted. These protocols resulted in samples with similar values of initial density and stress state but different values of initial

fabric, which were quantified by the initial mechanical coordination number z_{m0} and the contact normal-based fabric anisotropy a_{c0}. These samples are then subjected to constant-volume cyclic simple shearing to extract their liquefaction resistance. Observations from the results indicated that the liquefaction strength decreased following the order PA, PB, and PC for samples prepared at high relative density. Moreover, and the difference in liquefaction strength between PA (or PB) and PC increased with increasing D_r. This finding can be attributed to the decreasing z_{m0} or increasing a_{c0} observed in these samples. However, the pair (z_{m0}, a_{c0}) cannot fully explain the loose case, which may require additional exploration.

Acknowledgements

Financial support for this study was provided by the Natural Sciences and Engineering Research Council of Canada (NSERC). The authors thank Prof. E. Rathje for facilitating our access to high-performance computing resources at the Texas Advanced Computing Center.

References

Agnolin, I. and Roux, J.N. "Internal states of model isotropic granular packings. I. Assembling process, geometry, and contact networks". Physical Review E, 76(6), p.061302, 2007. https://doi.org/10.1103/PhysRevE.76.061302

Banerjee, S.K., Yang, M. and Taiebat, M. "Effect of coefficient of uniformity on cyclic liquefaction resistance of granular materials". Computers and Geotechnics, 155, p.105232, 2023. https://doi.org/10.1016/j.compgeo.2022.105232

Gu, X., Zhang, J. and Huang, X. "DEM analysis of monotonic and cyclic behaviors of sand based on critical state soil mechanics framework". Computers and Geotechnics, 128, p.103787, 2020. https://doi.org/10.1016/j.compgeo.2020.103787

Huang, X., Hanley, K.J., Zhang, Z. and Kwok, C.Y. "Structural degradation of sands during cyclic liquefaction: Insight from DEM simulations". Computers and Geotechnics, 114, p.103139, 2019. https://doi.org/10.1016/j.compgeo.2019.103139

Kloss, C., Goniva, C., Hager, A., Amberger, S. and Pirker, S. "Models, algorithms and validation for opensource DEM and CFD–DEM". Progress in Computational Fluid Dynamics, an International Journal, 12(2-3), pp.140-152, 2012. http://dx.doi.org/10.1504/PCFD.2012.047457

Mitchell, J.K. and Soga, K. "Fundamentals of soil behavior", Vol. 3, John Wiley & Sons, New York, USA, 2005.

Mulilis, J.P., Seed, H.B., Chan, C.K., Mitchell, J.K. and Arulanandan, K. "Effects of sample preparation on sand liquefaction". Journal of the Geotechnical Engineering Division, 103(2), pp. 91-108, 1977. https://doi.org/10.1061/AJGEB6.0000387

Mutabaruka, P., Taiebat, M., Pellenq, R.J.-M., and Radjai, F. (2019). "Effects of size polydispersity on random close-packed configurations of spherical particles." Physical Review E, 100(4), 042906. https://doi.org/10.1103/PhysRevE.100.042906

Ni, X., Ye, B., Zhang, F. and Feng, X. "Influence of specimen preparation on the liquefaction behaviors of sand and its mesoscopic explanation". Journal of Geotechnical and Geoenvironmental Engineering, 147(2), 04020161, 2021. https://doi.org/10.1061/(ASCE)GT.1943-5606.0002456

Ni, X., Zhang, Z., Ye, B. and Zhang, S. "Influence of anisotropy on liquefaction/reliquefaction resistance of granular materials and its quantitative evaluation". Soil Dynamics and Earthquake Engineering, 161, p.107415, 2022. https://doi.org/10.1016/j.soildyn.2022.107415

Oda, M. "Fabric tensor for discontinuous geological materials". Soils and foundations, 22(4), pp.96-108, 1982. http://dx.doi.org/10.3208/sandf1972.22.4_96

Oda, M., Kawamoto, K., Suzuki, K., Fujimori, H. and Sato, M. "Microstructural interpretation on reliquefaction of saturated granular soils under cyclic loading". Journal of Geotechnical and Geoenvironmental Engineering, 127(5), pp.416-423, 2001. https://doi.org/10.1061/(ASCE)1090-0241(2001)127:5(416)

Otsubo, M., Chitravel, S., Kuwano, R., Hanley, K.J., Kyokawa, H. and Koseki, J. "Linking inherent anisotropy with liquefaction phenomena of granular materials by means of DEM analysis". Soils and Foundations, 62(5), p.101202, 2022. https://doi.org/10.1016/j.sandf.2022.101202

Taiebat, M., Mutabaruka, P., Pellenq, R. and Radjai, F. "Effect of particle size distribution on 3D packings of spherical particles." In EPJ Web of Conferences, vol. 140, p. 02030. EDP Sciences, 2017. https://doi.org/10.1051/epjconf/201714002030

Tatsuoka, F., Muramatsu, M. and Sasaki, T. "Cyclic undrained stress-strain behavior of dense sands by torsional simple shear test". Soils and Foundations, 22(2), pp.55-70, 1982. https://doi.org/10.3208/sandf1972.22.2_55

Thornton, C. "Numerical simulations of deviatoric shear deformation of granular media". Géotechnique, 50(1), pp.43-53, 2000. https://doi.org/10.1680/geot.2000.50.1.43

Vaid, YP and Sivathayalan, S. "Fundamental factors affecting liquefaction susceptibility of sands". Canadian Geotechnical Journal , 37 (3), pp.592-606, 2000. https://doi.org/10.1139/t00-040

Wang, G. and Wei, J. "Microstructure evolution of granular soils in cyclic mobility and post-liquefaction process". Granular Matter, 18, pp. 1-13, 2016. https://doi.org/10.1007/s10035-016-0621-5

Wei, J. and Wang, G. "Discrete-element method analysis of initial fabric effects on pre-and post-liquefaction behavior of sands". Géotechnique Letters, 7(2), pp.161-166, 2017. http://dx.doi.org/10.1680/jgele.16.00147

Wood, F.M., Yamamuro, J.A. and Lade, P.V. "Effect of depositional method on the undrained response of silty sand". Canadian Geotechnical Journal, 45(11), pp.1525-1537, 2008. https://doi.org/10.1139/T08-079

Yamashita, S. and Toki, S. "Effects of fabric anisotropy of sand on cyclic undrained triaxial and torsional strengths". Soils and Foundations, 33(3), pp.92-104, 1993. https://doi.org/10.3208/sandf1972.33.3_92

Yang, M., Taiebat, M., Mutabaruka, P. and Radjaï, F. "Evolution of granular materials under isochoric cyclic simple shearing". Physical Review E, 103(3), 032904, 2021. https://doi.org/10.1103/PhysRevE.103.032904

Yang, M., Taiebat, M., Mutabaruka, P. and Radjaï, F. "Evolution of granular media under constant-volume multidirectional cyclic shearing". Acta Geotechnica, 17(3), pp.779-802, 2022a. https://doi.org/10.1007/s11440-021-01239-0

Yang, M., Taiebat, M. and Radjaï, F. "Liquefaction of granular materials in constant-volume cyclic shearing: Transition between solid-like and fluid-like states". Computers and Geotechnics, 148, p.104800, 2022b. https://doi.org/10.1016/j.compgeo.2022.104800

Yang, Z.X., Li, X.S. and Yang, J. "Quantifying and modelling fabric anisotropy of granular soils". Géotechnique, 58(4), 237-248, 2008. https://doi.org/10.1680/geot.2008.58.4.237

Zhang, A., Jiang, M. and Wang, D. "Effect of fabric anisotropy on the cyclic liquefaction of sands: Insight from DEM simulations". Computers and Geotechnics, 155, 105188, 2023. https://doi.org/10.1016/j.compgeo.2022.105188